Supporting Information

Pore control of Al-based MIL-53 isomorphs for the preferential capture of ethane in an ethane/ethylene mixture

Kyung Ho Cho[a,b], Ji Woong Yoon[a], Jeong Hyeon Lee[c], Jin Chul Kim[c], Kiwoong Kim[a], U-Hwang Lee[a], Minkee Choi[b]*, Sang Kyu Kwak[c]* and Jong-San Chang[a,d]*

[a]*Research Group for Nanocatalysts and Chemical & Process Technology Division, Korea Research Institute of Chemical Technology (KRICT), Gajeong-Ro 141, Yuseong, Daejeon 34114, Republic of Korea; E-mail: jschang@krict.re.kr*

[b]*Department of Chemical and Biomolecular Engineering, Korea Advanced Institute of Science and Technology (KAIST), Daejeon 34141, Republic of Korea; E-mail: mkchoi@kaist.ac.kr*

[c]*Department of Energy Engineering, School of Energy and Chemical Engineering, Ulsan National Institute of Science and Technology (UNIST), 50 UNIST-gil, Ulju-gun, Ulsan 44919, Republic of Korea; E-mail: skkwak@unist.ac.kr*

[d]*Department of Chemistry, Sungkyunkwan University, Suwon 440-476, Republic of Korea*

1. Characterization of materials

Powder X-ray diffraction (PXRD) patterns were recorded on a Rigaku D/MAX-2200/PC diffractometer using graphite-monochromated CuKα radiation (λ = 1.5418 Å). The XRD data were collected over the 2θ range from 3° to 40° with a step size of 0.02° and scan time of 4 s for each point at ambient temperature. High-temperature XRD data were measured on a Rigaku Ultima IVO equipped with a high-temperature cell under 30 cm^3 min^{-1} He flow. Scanning electron microscopy (SEM) images were obtained using a Tescan Mira 3 LMU FEG at 10 kV acceleration voltage, after coating the samples with Pt for 2 min in a Quorum Q 150T ES. Thermogravimetric analysis (TG) was carried out using a Scinco TGA i-1000 under 30 cm^3 min^{-1} N_2 flow with the ramping rate of 5 K min^{-1}. The C, H, N, and Al elemental compositions of the samples were determined by combining a Thermo Scientific FLASH 2000 series (EA analysis) and Thermo Scientific iCAP 6500 duo inductively coupled plasma-atomic emission spectrometer (ICP-AES).

2. Fitting of model equation of single component isotherms

The single-component C_2H_6 adsorption isotherms of all MIL-53 isomorphs and C_2H_4 adsorption isotherms of MIL-53-NDCA were fitted using the dual-site Langmuir-Freundlich (DSLF) model to obtain the best fitting results. The dual-site Langmuir-Freundlich (DSLF) equation is expressed by Eq. (S1):

$$q_i = q_{m1,i}\frac{K_{1,i}P^{n_A}}{1 + K_{1,i}P^{n_A}} + q_{m2,i}\frac{K_{2,i}P^{n_B}}{1 + K_{2,i}P^{n_B}},\ where\ K_{n,i} = K^0_{n,i}exp\left(-\frac{\Delta H_n}{RT}\right) \tag{S1}$$

where q_i is the uptake at equilibrium (mol kg^{-1}), R is the universal gas constant (J mol^{-1} K^{-1}), P is the equilibrium pressure (bar); $q_{m1,i}$ *and* $q_{m2,i}$ are the saturation capacities of sites 1 and 2 (mol kg^{-1}) of component i; $K^0_{1,i}$ and $K^0_{2,i}$ are the affinity coefficients of site 1 and 2 of component i (bar^{-1}); ΔH_n is energy parameter of site 1 and site 2 (kJ mol^{-1}); and n_A and n_B are equal to $1/n_1$ and $1/n_2$, respectively, where n_1 and n_2 are the respective deviations from the ideal homogeneous surface. The single-component C_2H_4 adsorption isotherms of MIL-53-BDC and MIL-BPDC were fitted using the Langmuir-Freundlich (LF) model Eq. (S2):

$$q_i = q_{m1,i}\frac{K_{1,i}P^{n_A}}{1 + K_{1,i}P^{n_A}},\ where\ K_{n,i} = K^0_{n,i}exp\left(-\frac{\Delta H_n}{RT}\right) \tag{S2}$$

3. Isotsteric heats of adsorption

The isosteric heat of adsorption was calculated from the isotherms collected at three different temperatures (273, 283 and 293 K) by Eq. (S3):

$$Q_{st} = R\left(\frac{\partial ln\, P}{\partial\left(\frac{1}{T}\right)}\right)_q \tag{S3}$$

where Q_{st} is the isosteric heat of adsorption (kJ mol^{-1}), R is the universal gas constant (J mol^{-1} K^{-1}), P and T represent pressure (bar) and temperature (K), respectively, and q is the adsorption amount per weight of the adsorbent (mol kg^{-1}).

4. Prediction of IAST selectivity

The ideal adsorbed solution theory (IAST) was developed by Myers and Prausnitz to predict the adsorption equilibria in multi-component gas mixture adsorption.[1,2] The adsorption parameters calculated using the DSLF or LF equation were used for the calculation of the IAST selectivity, as expressed in Eq. (S4):

$$S = \frac{X_1}{X_2} \times \frac{Y_2}{Y_1} \tag{S4}$$

,where X_1 and X_2 are the mole fractions of the adsorbed C_2H_6 and C_2H_4, respectively, while Y_1 and Y_2 are the partial pressures of the C_2H_6 and C_2H_4 in a gas mixture.

5. Productivity of C_2H_4

Because the total gas flow rate changes during the breakthrough experiment due to the dynamic adsorption/desorption of C_2H_6 and C_2H_4, the time-dependent gas flow rate was separately recorded using a mass flow meter (see the breakthrough setup in Fig. S8). Then, it was multiplied with the time-dependent C/C_0 profiles (Fig. 5) to calculate the absolute amount of flowed C_2H_6 and C_2H_4 (Fig. S10). The C_2H_4 productivity was defined by the breakthrough amount of ethylene (defined as a volume of gas at STP) over an adsorbent bed packed with 1 kg of MOF. The breakthrough amount was calculated by the integration of the breakthrough curves during a period from t_1 to t_2 during which the C_2H_4 purity is kept higher than a threshold value of 99.95%. The productivity of C_2H_4 is expressed by Eq. (S5)

$$Productivity\ of\ C_2H_4\ (\frac{L}{kg}) = \frac{\int_{t_1}^{t_2} F_{C2H4}\, dt}{Weight\ of\ adsorbent} \tag{S5}$$

, where F_{C2H4} is the outlet flow rate of C_2H_4.

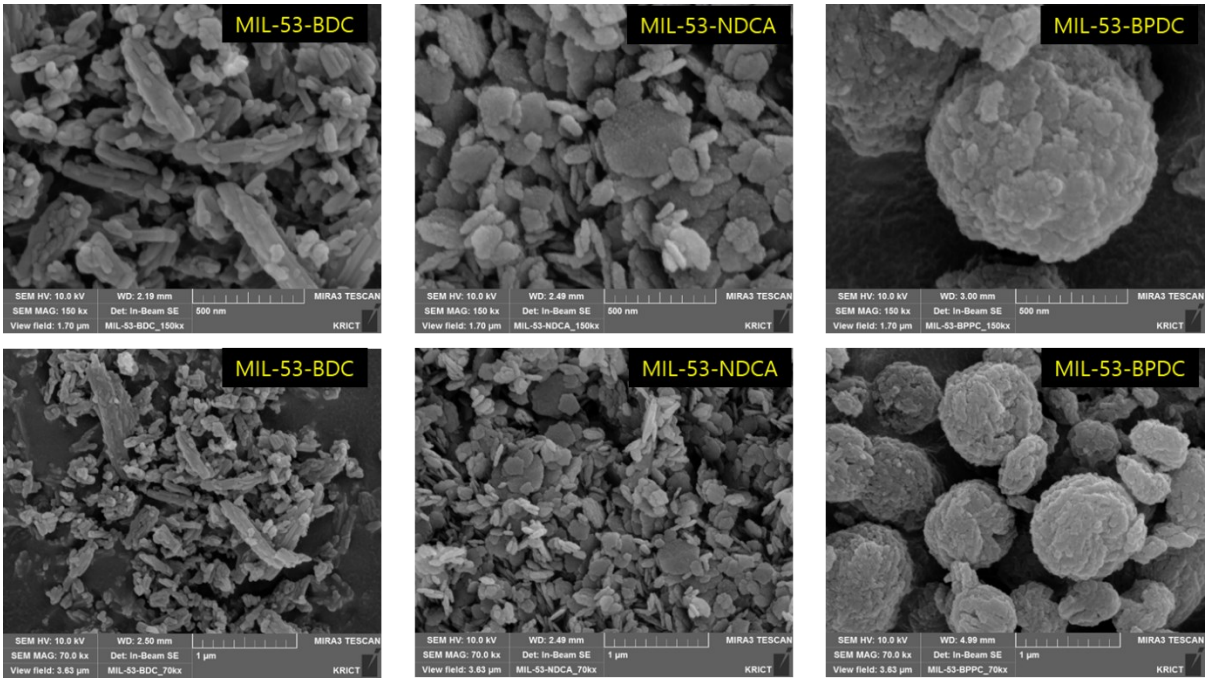

Figure S1. Scanning electron microscopy (SEM) images of MIL-53 isomorphs.

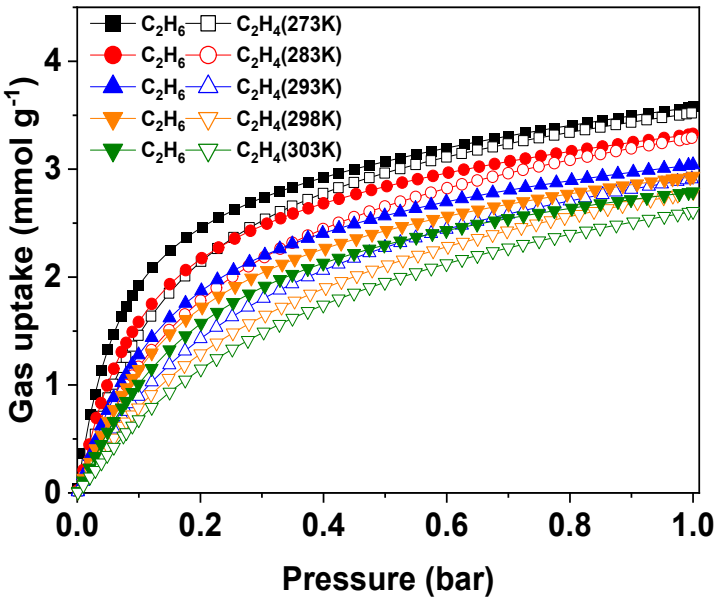

Figure S2. Single-component C_2H_6 and C_2H_4 adsorption isotherms of MIL-53-BDC at five different temperatures (273–303 K).

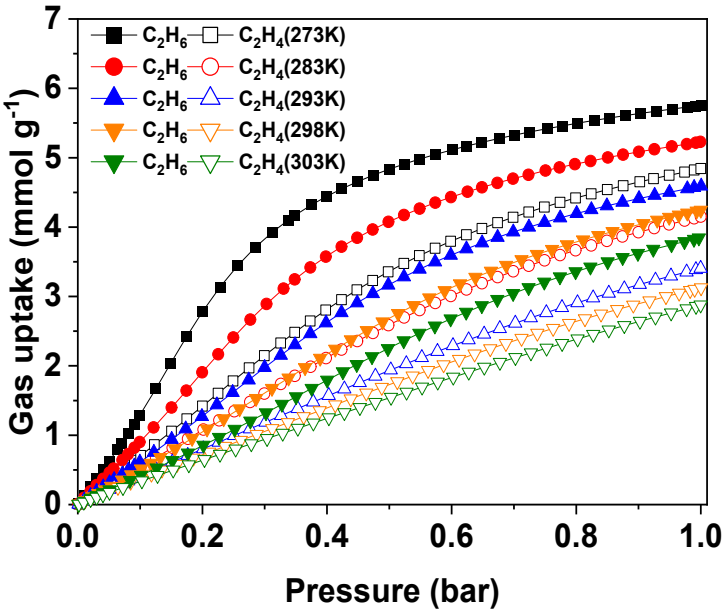

Figure S3. Single-component C_2H_6 and C_2H_4 adsorption isotherms of MIL-53-NDCA at five different temperatures (273–303 K).

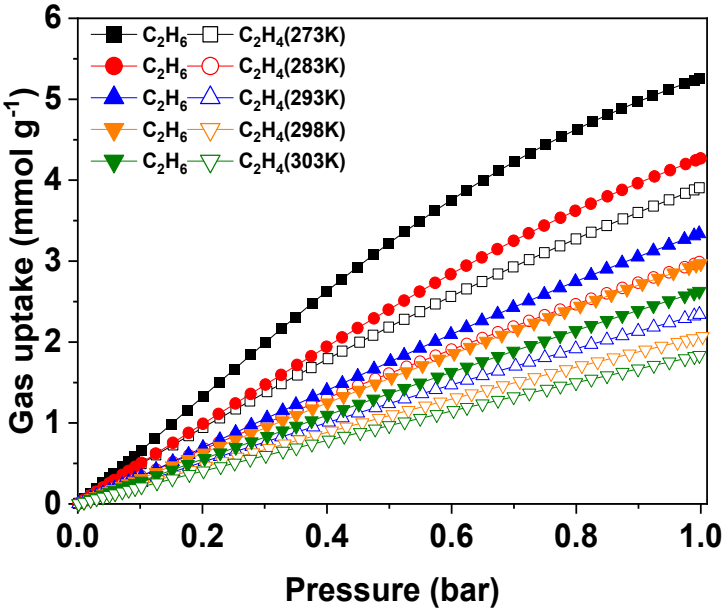

Figure S4. Single-component C_2H_6 and C_2H_4 adsorption isotherms of MIL-53-BPDC at five different temperatures (273–303 K).

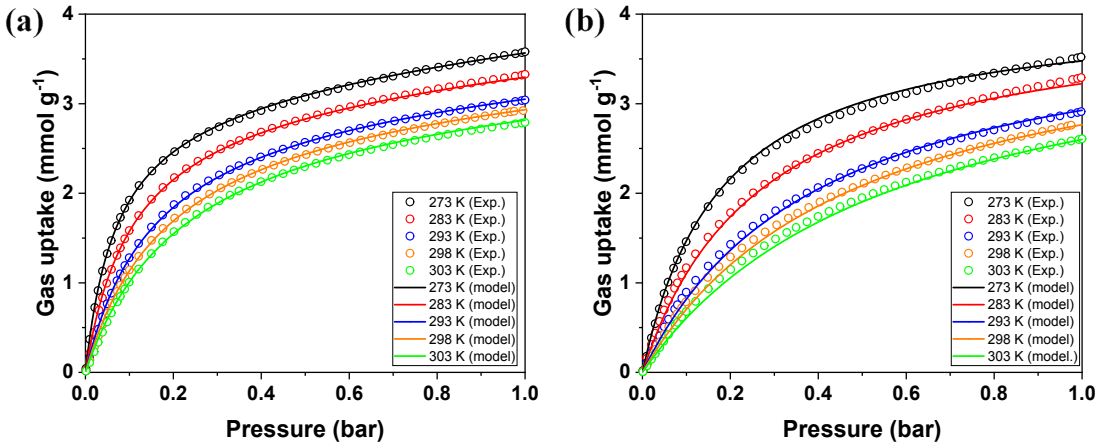

Figure S5. (a) The fitting results of the C_2H_6 isotherms of MIL-53-BDC with the dual-site Langmuir-Freundlich (DSLF) model. (b) The fitting results of the C_2H_4 isotherms of MIL-53-BDC with the Langmuir-Freundlich (LF) model.

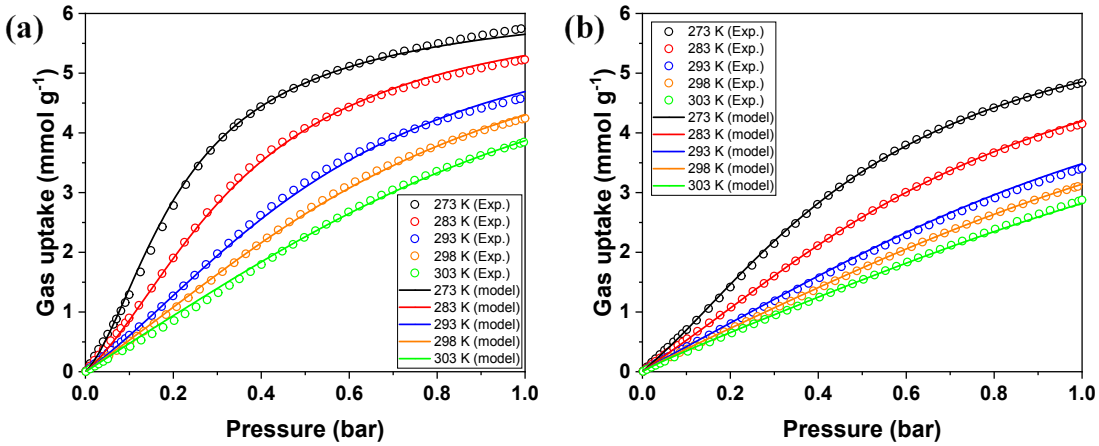

Figure S6. (a) The fitting results of the C_2H_6 isotherms and (b) the C_2H_4 isotherms of MIL-53-NDCA with the dual-site Langmuir-Freundlich (DSLF) model.

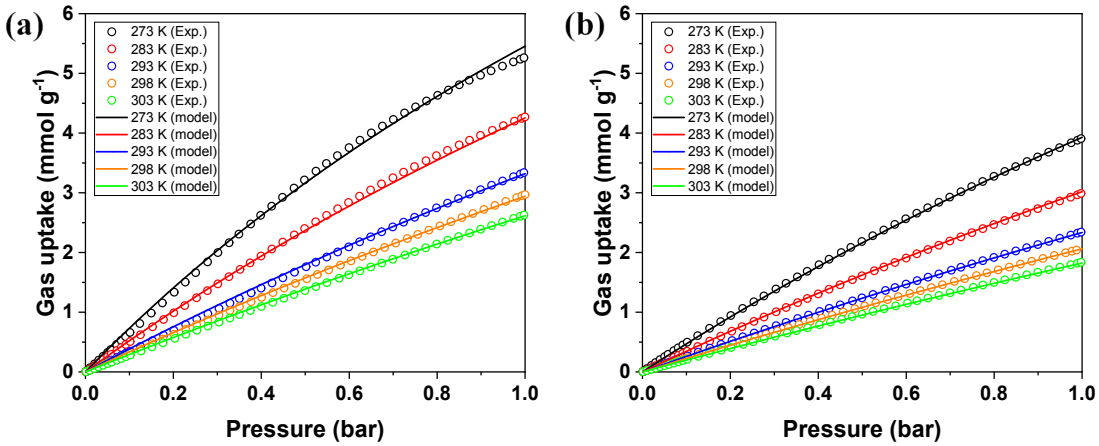

Figure S7. (a) The fitting results of the C_2H_6 isotherms of MIL-53-BPDC with the dual-site Langmuir-Freundlich (DSLF) model. (b) The fitting results of the C_2H_4 isotherms of MIL-53-BPDC with the Langmuir-Freundlich (LF) model.

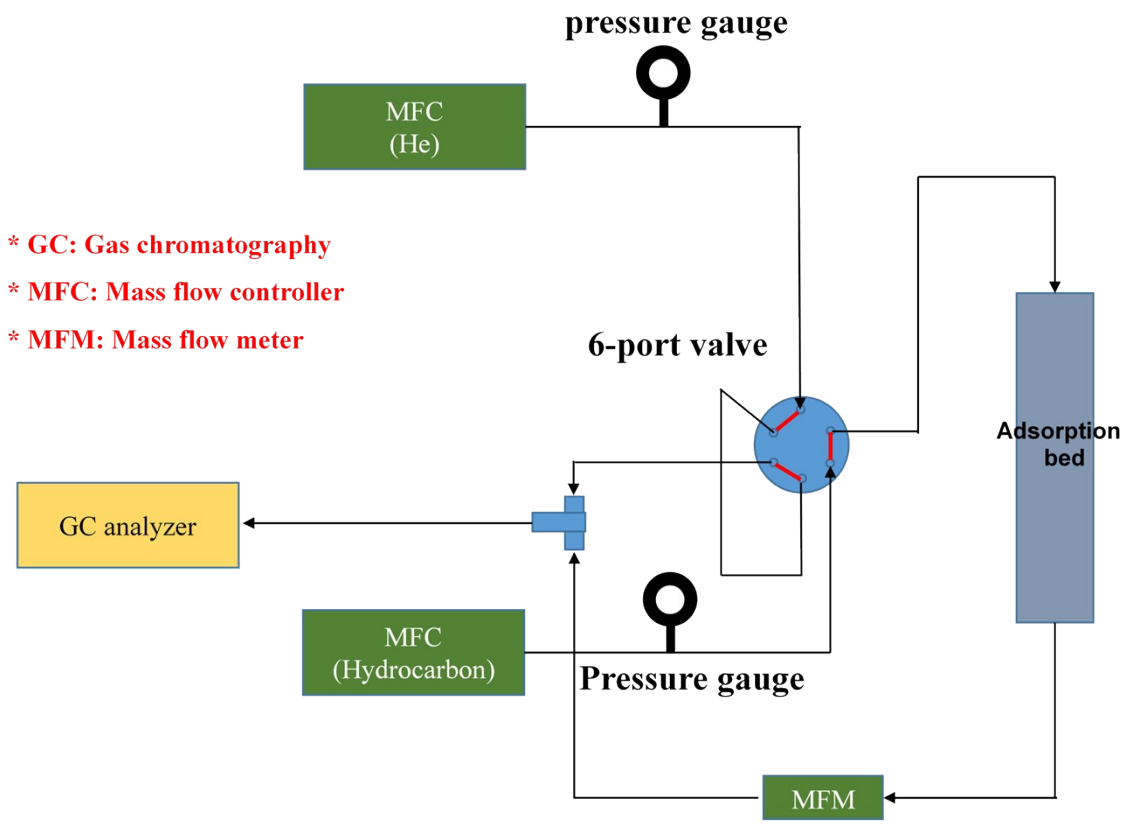

Figure S8. Schematic representation of the breakthrough setup.

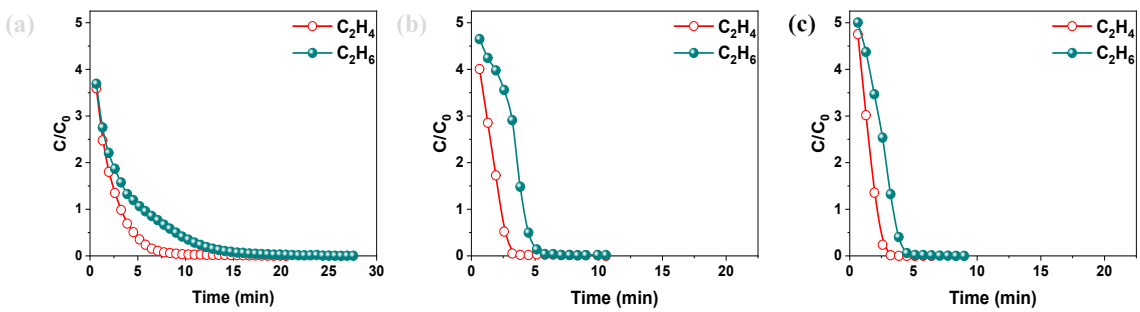

Figure S9. C_2H_4 and C_2H_6 desorption profiles of (a) MIL-53-BDC, (b) MIL-53-NDCA, and (c) MIL-53-BPDC at 298 K under a He flow (30 cm^3 min^{-1}).

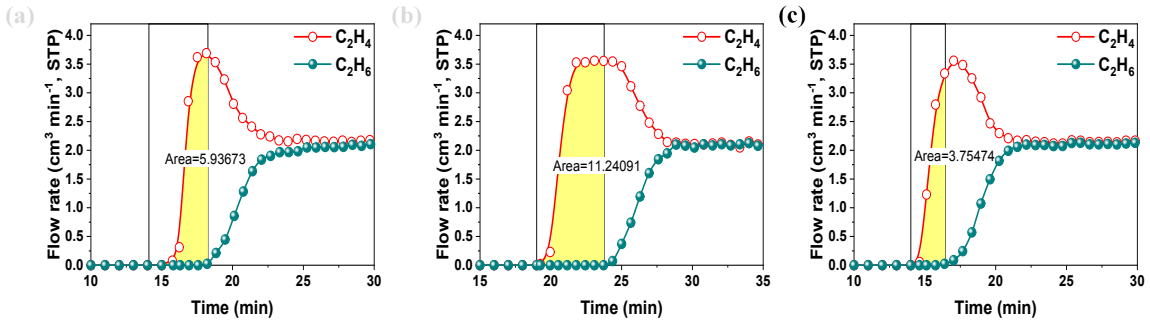

Figure S10. Outlet flow rate (the gas volume is based on STP) of C_2H_6 and C_2H_4 in the breakthrough experiments with (a) MIL-53-BDC, (b) MIL-53-NDCA, and (c) MIL-53-BPDC. The integrated area (yellow) represents the produced volume of high-purity C_2H_4 (>99.95%).

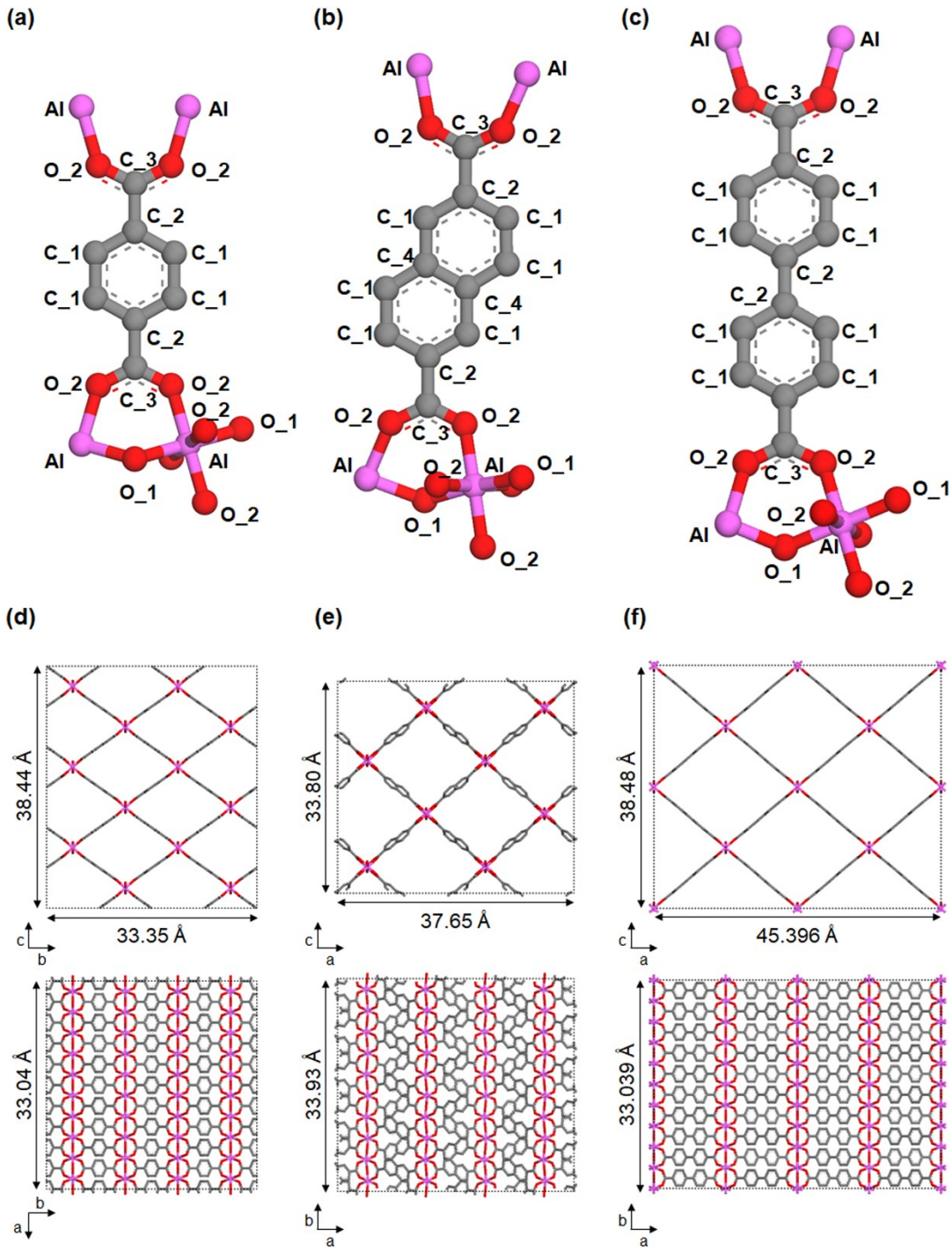

Figure S11. Atom types of potential energy parameters consisting of (a) MIL-53-BDC, (b) MIL-53-NDCA, and (c) MIL-53-BPDC. Front (*top*) and top (*bottom*) views of GCMC simulation models of (d) MIL-53-BDC, (e) MIL-53-NDCA, and (f) MIL-53-BPDC. Carbon, oxygen, and aluminum atoms are colored in grey, red, and pink, respectively.

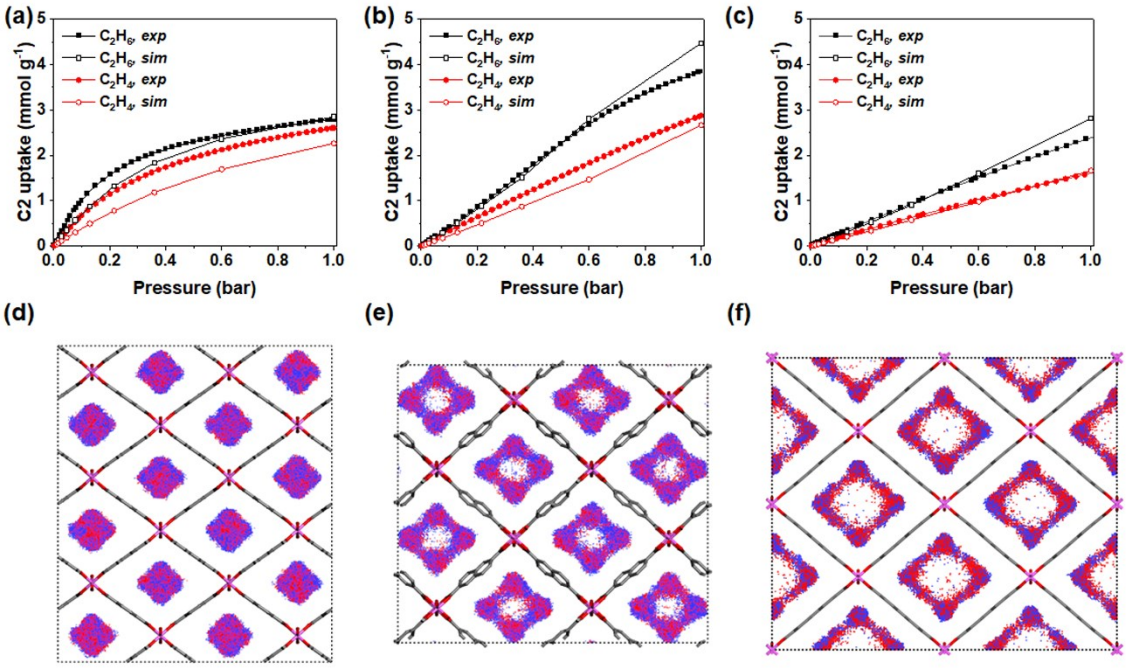

Figure S12. Adsorption isotherms of C_2H_6 and C_2H_4 on (a) MIL-53-BDC, (b) MIL-53-NDCA, and (c) MIL-53-BPDC at 303 K. The experimental (closed symbol) and simulation (open symbol) adsorption isotherms are compared. Density fields of adsorbed C_2H_6 (red dots) and C_2H_4 (blue dots) on (d) MIL-53-BDC, (e) MIL-53-NDCA, and (f) MIL-53-BPDC at 303 K and 1 bar. For (d), (e), and (f), carbon, oxygen, and aluminum atoms are colored in grey, red, and pink, respectively.

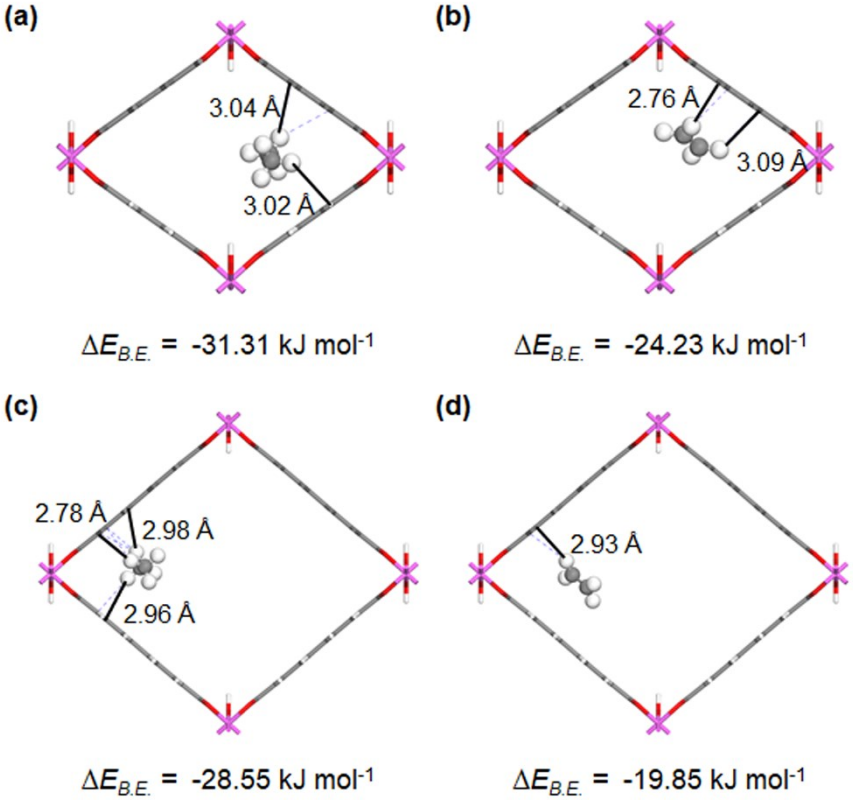

Figure S13. Optimized configurations and binding energies of (a) C_2H_6 and (b) C_2H_4 at Site **I** in MIL-53-BDC and (c) C_2H_6 and (d) C_2H_4 at Site **I** in MIL-53-BPDC. Carbon, hydrogen, oxygen, and aluminum atoms are colored in grey, white, red, and pink, respectively.

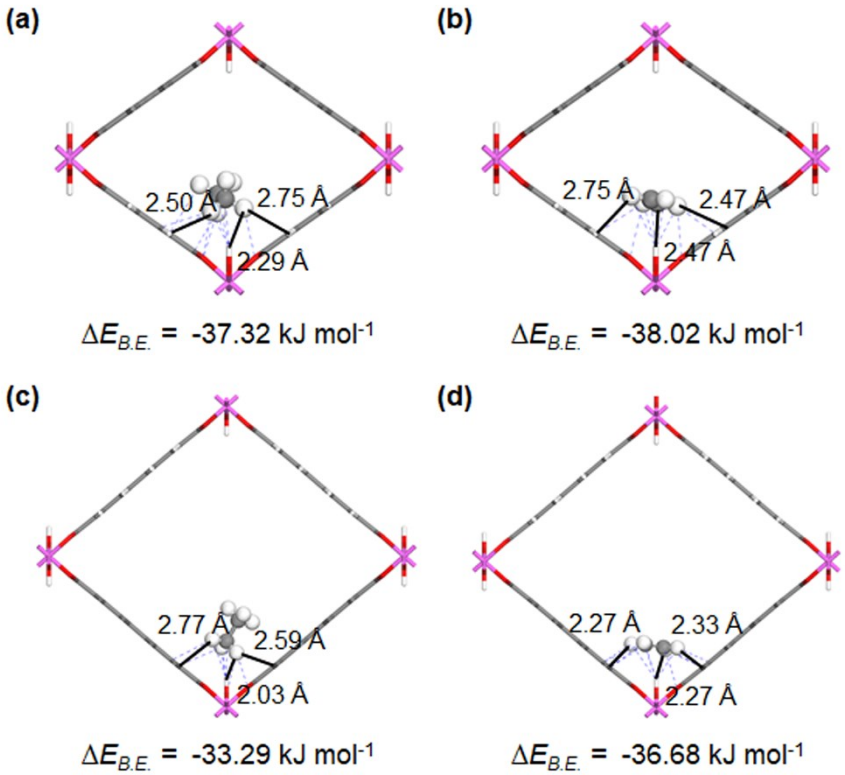

Figure S14. Optimized configurations and binding energies of (a) C_2H_6 and (b) C_2H_4 at Site **II** in MIL-53-BDC and (c) C_2H_6 and (d) C_2H_4 at Site **II** in MIL-53-BPDC. Carbon, hydrogen, oxygen, and aluminum atoms are colored in grey, white, red, and pink, respectively**.**

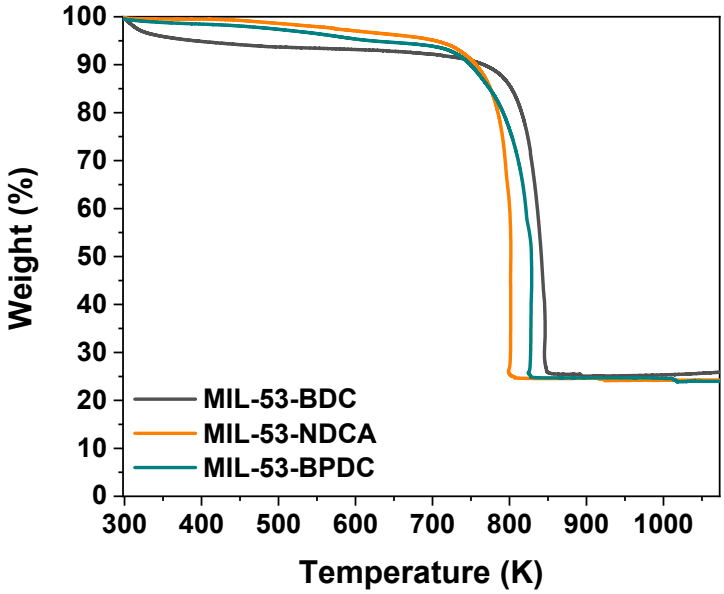

Figure S15. Thermogravimetric analysis of MIL-53 isomorphs under N_2 (temperature ramp: 5 K min^{-1}).

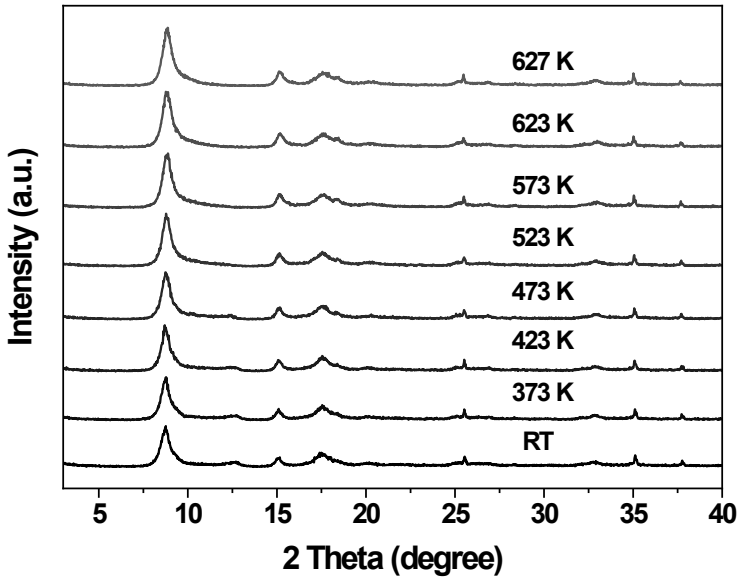

Figure S16. High-temperature PXRD patterns of MIL-53-BDC measured under 30 cm^3 min^{-1} He flow.

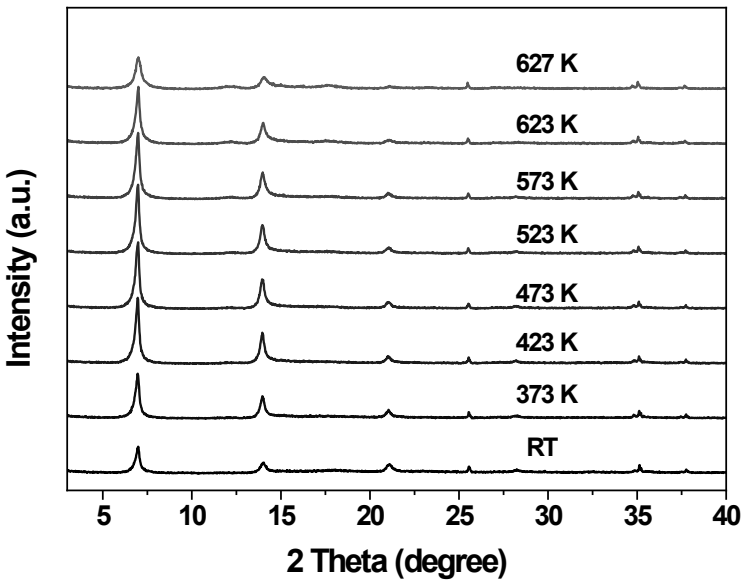

Figure S17. High-temperature PXRD patterns of MIL-53-NDCA measured under 30 cm^3 min^{-1} He flow.

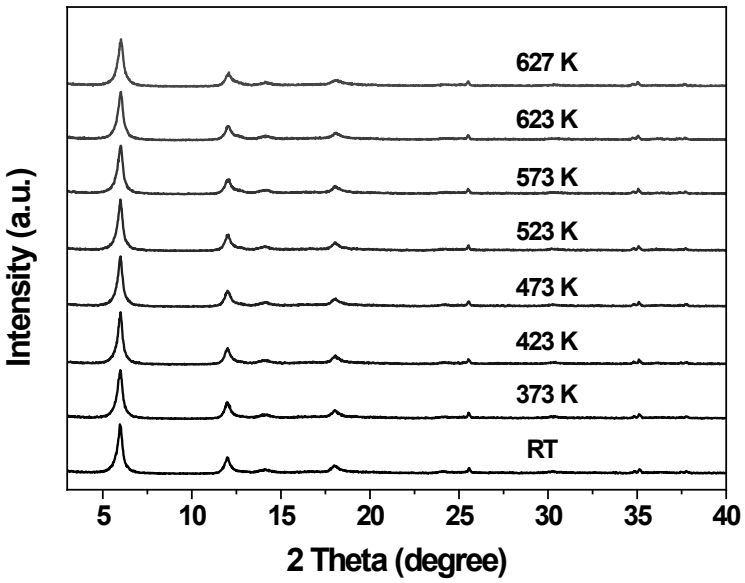

Figure S18. High-temperature PXRD patterns of MIL-53-BPDC measured under 30 cm^3 min^{-1} He flow.

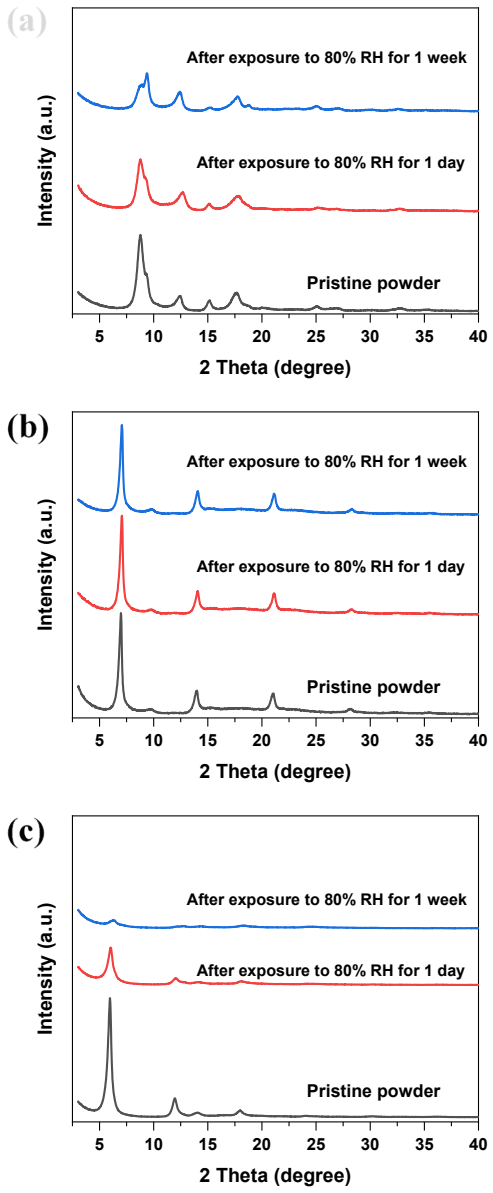

Figure S19. PXRD patterns of (a) MIL-53-BDC, (b) MIL-53-NDCA and (c) MIL-53-BPDC after exposure to 80% relative humidity at 298 K.

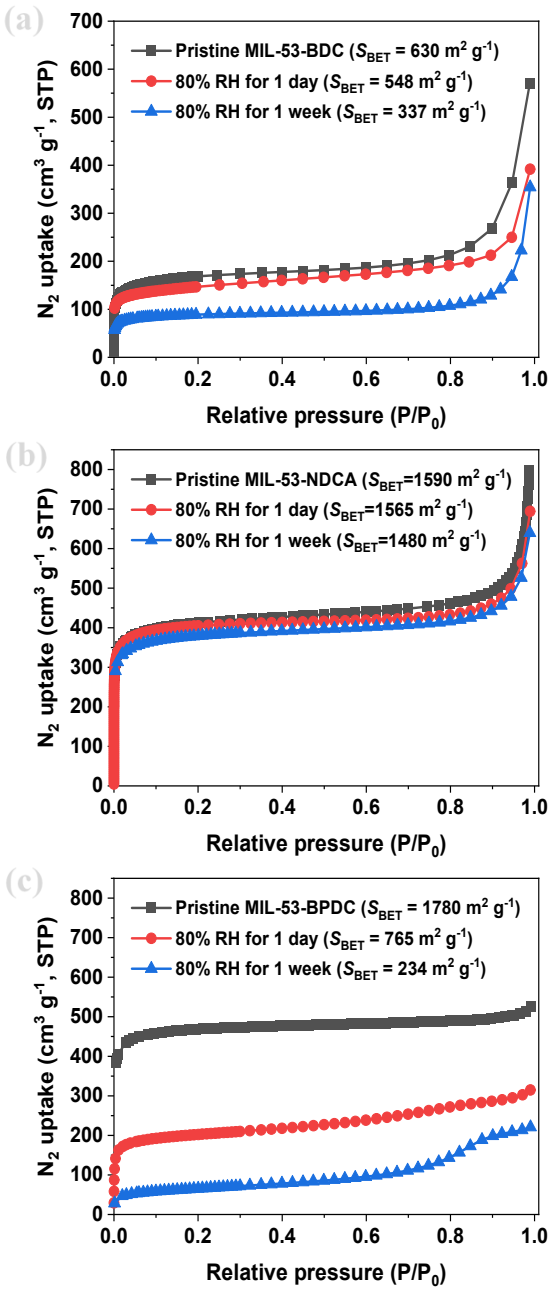

Figure S20. N_2 adsorption isotherms of (a) MIL-53-BDC, (b) MIL-53-NDCA, and (C) MIL-53-BPDC after exposure to 80% relative humidity at 298 K.

Table S1. Theoretical/experimentally determined chemical compositions (using EA and ICP) and pore structural properties of the MIL-53 isomorphs.

Samples	Theoretical composition (wt%)			Experimentally determined composition (wt%)				Structural formula	S_{BET}[a] ($m^2\ g^{-1}$)	V_{micro}[b] ($cm^3\ g^{-1}$)
	Al	C	H	Al	C	H	N			
MIL-53-BDC	12.97	46.2	2.4	13.3	43.34	2.61	0.36	$Al(OH)(BDC)_{0.92}$	630	0.222
MIL-53-NDCA	10.45	55.83	2.71	10.8	54.78	2.79	0.21	$Al(OH)(NDCA)_{0.952}$	1590	0.584
MIL-53-BPDC	9.49	59.16	3.17	10.5	57.71	3.16	0.08	$Al(OH)(BPDC)_{0.88}$	1780	0.614

[a]Specific surface area (S_{BET}) was calculated using the Brunauer–Emmett–Teller (BET) equation. [b]The micropore volume (V_{micro}) was calculated using the *t*-plot method.

Table S2. Fitting results of the C_2H_6 and C_2H_4 adsorption isotherms of the MIL-53 isomorphs using the DSLF and LF models, respectively.

Samples	Adsorbate	q_m (mol kg^{-1})		$K^0_{n,i}$ (bar^{-1})		$-\Delta H$ (kJ mol^{-1})		n	
		q_{m1}	q_{m2}	$K^0_{1,i}$	$K^0_{2,i}$	$(-\Delta H_1)$	$(-\Delta H_2)$	n_A	n_B
MIL-53-BDC	C_2H_6	3.11	3.75	1.47×10^{-4}	5.38×10^{-6}	26.08	24.03	1	1
	C_2H_4	4.10	-	4.09×10^{-5}	-	26.84	-	1	-
MIL-53-NDCA	C_2H_6	3.91	2.56	1.60×10^{-11}	3.91×10^{-2}	63.16	9.91	1.87	1.02
	C_2H_4	4.71	1.82	9.57×10^{-8}	3.91×10^{-2}	39.3	9.29	1.68	0.92
MIL-53-BPDC	C_2H_6	6.73	16.4	9.13×10^{-7}	3.44×10^{-4}	30.42	14.63	1	1
	C_2H_4	21.54	-	3.07×10^{-5}	-	20.18	-	1	-

Table S3. Comparison of various adsorbents in terms of C_2H_6 and C_2H_4 adsorption capacity, C_2H_6/C_2H_4 selectivity, isosteric heat of adsorption, and C_2H_4 productivity over 99.95% purity at 1 bar.

Adsorbent	T (K)	q_{C2H6} (mmol g^{-1})	q_{C2H4} (mmol g^{-1})	Selectivity[a]	$-Q_{st,\ C2H6}$ (kJ mol^{-1})	$-Q_{st,C2H4}$ (kJ mol^{-1})	Productivity of C_2H_4 (99.95%)[d]	Ref.
ZIF-7	298	1.83	1.80	1.5	-	-	2	3
ZIF-8	293	2.52	1.51	1.7	-	-	0.4	4
ZIF-4	298	2.3	2.2	2.15	-	-	6.6	5
IRMOF-8	298	4.5	3.1	1.78	52.5	49.5	-	6
MAF-49	316	1.7	1.7	2.7	56.7	45.5	5.3	7
MIL-142A	298	3.8	2.9	1.5	25.1	23.8	6.7	8
BasoliteA100	303	2.5	1.6	1.65	29.0	27.0	-	9
MIL-53-FA	308	3.7	3.35	1.9	29.0	27.0	-	10
Fe_2O_2(DOBDC)	298	3.3	2.6	4.4	66.8	37.0	19.3	11
PCN-245	298	3.27	2.39	1.9[b]	23.0	20.5	5.8	12
PCN-250	298	5.21	4.22	1.9	23.6	21.1	10	13
MUF-15	293	4.69	4.15	1.95	37.5	33.0	14.0	14
$Cu(Qc)_2$	298	1.9	0.8	3.7	29.0	25.4	4.34	15
UTSA-35a	296	2.43	2.16	1.4	29.0	28.9	-	16
UiO-66-ADC	298	1.6	1.7	1.8	36.0	36.0	-	17
UiO-66-2CF_3	318	0.6	0.5	2.5	28.0	5.0	-	18
NiBDC$(TED)_{0.5}$	293	5.00	3.4	1.6	21.5	18.5	-	19
NiTMBDC$(TED)_{0.5}$	298	5.45	5.02	1.99[c]	39	32	-	20
ZJU-120a	296	4.91	3.93	2.74	27.6	26.5	8.39	21
CPM-733	298	7.12	6.37	1.75	23.3	22.5	19.71	22
MIL-53-BDC	298	2.93	2.78	1.70	27.2	22.3	5.3	This work
MIL-53-NDCA	298	4.24	3.12	1.53	24.2	17.0	11.2	This work
MIL-53-BPDC	298	2.97	2.07	1.47	22.1	22.1	3.5	This work

[a] Selectivity calculated by IAST for an equimolar mixture of C_2H_6/C_2H_4 at 1 bar

[b] For C_2H_6/C_2H_4 (1/9 v/v)

[c] For C_2H_6/C_2H_4 (1/15 v/v)

[d] Calculated based on the breakthrough experiments using a C_2H_6/C_2H_4 (50/50 v/v) mixture gas

Table S4. Potential energy parameters of Lennard-Jones 12-6 potential, $E(R) = D_0\left(\left(\frac{R_0}{R}\right)^{12} - 2\left(\frac{R_0}{R}\right)^{6}\right)$, adopted from TraPPE-UA. Atom types are corresponding to **Fig. S11a–c**.

Atom type	R_0 (Å)	D_0 (kcal/mol)	Ref.
Al	0	0	23
O_1	3.3898	0.1848	24
O_2	3.1429	0.1093	25
C_1	4.1475	0.1004	26
C_2	4.3552	0.0417	26
C_3	4.3215	0.0397	27
C_4	4.1531	0.0596	26
C_CH_3	4.2092	0.1947	28
C_CH_2	4.125	0.1689	26

References

1. A. L. Myers and J. M. Prausnitz, *AlChE J.*, 1965, **11**, 121.
2. S. J. Caldwell, B. Al-Duri, N. Sun, C.-g. Sun, C. E. Snape, K. Li and J. Wood, *Energy Fuels*, 2015, **29**, 3796.
3. C. Gücüyener, J. van den Bergh, J. Gascon and F. Kapteijn, *J. Am. Chem. Soc.*, 2010, **132**, 17704.
4. U. Bohme, B. Barth, C. Paula, A. Kuhnt, W. Schwieger, A. Mundstock, J. Caro and M. Hartmann, *Langmuir*, 2013, **29**, 8592.
5. M. Hartmann, U. Bohme, M. Hovestadt and C. Paula, *Langmuir*, 2015, **31**, 12382.
6. J. Pires, M. L. Pinto and V. K. Saini, *ACS Appl. Mater. Interfaces*, 2014, **6**, 12093.
7. P. Q. Liao, W. X. Zhang, J. P. Zhang and X. M. Chen, *Nat. Commun.*, 2015, **6**, 8697.
8. Y. Chen, H. Wu, D. Lv, R. Shi, Y. Chen, Q. Xia and Z. Li, *Ind. Eng. Chem. Res.*, 2018, **57**, 4063.
9. R. P. P. L. Ribeiro, B. C. R. Camacho, A. Lyubchyk, I. A. A. C. Esteves, F. J. A. L. Cruz and J. P. B. Mota, *Micropor. Mesopor. Mater.*, 2016, **230**, 154.
10. J. Peng, Y. Sun, Y. Wu, Z. Lv and Z. Li, *Ind. Eng. Chem. Res.*, 2019, **58**, 8290.
11. L. Li, R. B. Lin, R. Krishna, H. Li, S. Xiang, H. Wu, J. Li, W. Zhou and B. Chen, *Science*, 2018, **362**, 443.
12. D. Lv, R. Shi, Y. Chen, Y. Wu, H. Wu, H. Xi, Q. Xia and Z. Li, *ACS Appl. Mater. Interfaces*, 2018, **10**, 8366.
13. Y. Chen, Z. Qiao, H. Wu, D. Lv, R. Shi, Q. Xia, J. Zhou and Z. Li, *Chem. Eng. Sci.*, 2018, **175**, 110.
14. O. T. Qazvini, R. Babarao, Z. L. Shi, Y. B. Zhang and S. G. Telfer, *J. Am. Chem. Soc.*, 2019, **141**, 5014.
15. R. B. Lin, H. Wu, L. Li, X. L. Tang, Z. Li, J. Gao, H. Cui, W. Zhou and B. Chen, *J. Am. Chem. Soc.*, 2018, **140**, 12940.
16. Y. He, Z. Zhang, S. Xiang, F. R. Fronczek, R. Krishna and B. Chen, *Chem. Commun.*, 2012, **48**, 6493.
17. Y. Wang, S. Yuan, Z. Hu, T. Kundu, J. Zhang, S. B. Peh, Y. Cheng, J. Dong, D. Yuan, H.-C. Zhou and D. Zhao, *ACS Sustain. Chem. Eng.*, 2019, **7**, 7118.
18. J. Pires, J. Fernandes, K. Dedecker, J. R. B. Gomes, G. Perez-Sanchez, F. Nouar, C. Serre and M. L. Pinto, *ACS Appl. Mater. Interfaces*, 2019, **11**, 27410.
19. H. Xiang, A. Ameen, P. Gorgojo, F. R. Siperstein, S. M. Holmes and X. Fan, *Micropor. Mesopor. Mater.*, 2020, **292,** 109724
20. X. Wang, Z. Niu, A. M. Al-Enizi, A. Nafady, Y. Wu, B. Aguila, G. Verma, L. Wojtas, Y.-S. Chen, Z. Li and S. Ma, *J. Mater. Chem. A*, 2019, **7**, 13585.
21. J. Pei, J.-X. Wang, K. Shao, Y. Yang, Y. Cui, H. Wu, W. Zhou, B. Li and G. Qian, *J. Mater. Chem. A*, 2020, **8**, 3613.
22. H. Yang, Y. Wang, R. Krishna, X. Jia, Y. Wang, A. N. Hong, C. Dang, H. E. Castillo, X. Bu and P. Feng, *J. Am. Chem. Soc.*, 2020, **142**, 2222.
23. N. A. Ramsahye, G. Maurin, S. Bourrelly, P. L. Llewellyn, T. Loiseau, C. Serre and G. Férey, *Chem. Commun.*, 2007, DOI: 10.1039/B702986A, 3261.
24. B. Chen, J. J. Potoff and J. I. Siepmann, *J. Phys. Chem. B*, 2001, **105**, 3093.
25. J. M. Stubbs, J. J. Potoff and J. I. Siepmann, *J. Phys. Chem. B*, 2004, **108**, 17596.
26. C. D. Wick, M. G. Martin and J. I. Siepmann, *J. Phys. Chem. B*, 2000, **104**, 8008.
27. G. Kamath, F. Cao and J. J. Potoff, *J. Phys. Chem. B*, 2004, **108**, 14130.
28. M. G. Martin and J. I. Siepmann, *J. Phys. Chem. B*, 1998, **102**, 2569.